

Article

Demarcation Line Determination for Diagnosis of Gastric Cancer Disease Range Using Unsupervised Machine Learning in Magnifying Narrow-Band Imaging

Shunsuke Okumura ¹, Misa Goudo ¹, Satoru Hiwa ^{2,*}, Takeshi Yasuda ³, Hiroaki Kitae ³, Yuriko Yasuda ³, Akira Tomie ³, Tatsushi Omatsu ³, Hiroshi Ichikawa ⁴, Nobuaki Yagi ³ and Tomoyuki Hiroyasu ²

¹ Graduate School of Life and Medical Sciences, Doshisha University, Kyoto 610-0394, Japan

² Department of Biomedical Sciences and Informatics, Doshisha University, 1-3 Tatara Miyakodani, Kyotanabe, Kyoto 610-0394, Japan

³ Department of Gastroenterology, Asahi University Hospital, Gifu 500-8523, Japan

⁴ Department of Medical Life Systems, Doshisha University, Kyoto 610-0394, Japan

* Correspondence: shiwa@mail.doshisha.ac.jp

Citation: Okumura, S.; Goudo, M.; Hiwa, S.; Yasuda, T.; Kitae, H.; Yasuda, Y.; Tomie, A.; Omatsu, T.; Ichikawa, H.; Yagi, N.; et al. Demarcation Line Determination for Diagnosis of Gastric Cancer Disease Range Using Unsupervised Machine Learning in Magnifying Narrow-Band Imaging. *Diagnostics* **2022**, *12*, 2491. <https://doi.org/10.3390/diagnostics12102491>

Academic Editors: Takayuki Ando and Ayumu Hosokawa

Received: 12 September 2022

Accepted: 11 October 2022

Published: 14 October 2022

Publisher's Note: MDPI stays neutral with regard to jurisdictional claims in published maps and institutional affiliations.



Copyright: © 2022 by the authors. Licensee MDPI, Basel, Switzerland. This article is an open access article distributed under the terms and conditions of the Creative Commons Attribution (CC BY) license (<https://creativecommons.org/licenses/by/4.0/>).

Abstract: Background and Aims: It is important to determine an accurate demarcation line (DL) between the cancerous lesions and background mucosa in magnifying narrow-band imaging (M-NBI)-based diagnosis. However, it is difficult for novice endoscopists. We aimed to automatically determine the accurate DL using a machine learning method. Methods: We used an unsupervised machine learning approach to determine the DLs. Our method consists of the following four steps: (1) an M-NBI image is segmented into superpixels using simple linear iterative clustering; (2) the image features are extracted for each superpixel; (3) the superpixels are grouped into several clusters using the *k*-means method; and (4) the boundaries of the clusters are extracted as DL candidates. The 23 M-NBI images of 11 cases were used for performance evaluation. The evaluation investigated the similarity of the DLs identified by endoscopists and our method, and the Euclidean distance between the two DLs was calculated. For the single case of 11 cases, the histopathological examination was also conducted to evaluate the proposed system. Results: The average Euclidean distances for the 11 cases were 10.65, 11.97, 7.82, 8.46, 8.59, 9.72, 12.20, 9.06, 22.86, 8.45, and 25.36. The results indicated that the proposed method could identify similar DLs to those identified by experienced doctors. Additionally, it was confirmed that the proposed system could generate pathologically valid DLs by increasing the number of clusters. Conclusions: Our proposed system can support the training of inexperienced doctors as well as enrich the knowledge of experienced doctors in endoscopy.

Keywords: computer-aided diagnosis; gastrointestinal endoscopy; gastric cancer; diagnostic and therapeutic endoscopy; unsupervised machine learning; magnifying narrow-band imaging

1. Introduction

Several studies have reported that magnifying narrow-band imaging (M-NBI) is useful for diagnosing the existence of early gastric cancer and determining its horizontal extent [1–3]. The detected cancer lesions can subsequently be removed endoscopically using endoscopic submucosal dissection (ESD) [4,5].

However, ESD demonstrates certain matters of concern, such as complications and the risk of non-curative resection (remnants of cancer) [6–8]. Although this is also the case for other endoscopic procedures, accidental perforation sometimes occurs [9–11]. Furthermore, the incorrect recognition of the demarcation line (DL) is disadvantageous to patients. When endoscopists underestimate the DL, this may lead to non-curative resection. In contrast, if they overestimate the DL, they may perform ESD containing extensive

unnecessary lesions, increasing the risk of perforation or long procedure time. Therefore, it is important to determine an accurate DL between the cancerous lesions and background mucosa. However, this determination is difficult for novice endoscopists with the required long-term training and experience.

With the recent development of machine learning (ML) technology, computer-aided diagnosis (CAD) systems are playing an increasingly important role in the medical field and are expected to aid endoscopists with accurate and stable disease detection and diagnosis. In the gastroenterology field, CAD systems for the detection of esophageal cancer, gastric cancer, *H. pylori* infection, and the characterization of colorectal lesions have been developed and validated for clinical use [12–15].

In this study, we developed a new CAD system that automatically determines the DL on a given M-NBI image through an ML method.

The main objectives of the proposed system are to provide the DL candidates for diagnosis of the disease range of early gastric cancer to endoscopists, as well as to support the accurate and stable diagnosis. In recent years, research on image diagnosis using supervised ML such as deep learning has attracted significant interest in medicine owing to its higher classification and prediction performance compared to conventional methods [12,13,16,17]. However, disadvantages exist in obtaining high-performance results with these methods. First, it is necessary to prepare an enormous amount of annotated training data (for example, ‘lesion’ or ‘non-lesion’ labels are provided to each datum by endoscopists) to construct the classification model. These annotations need to be performed by highly experienced endoscopists and are therefore impractical. Second, the diagnosis rationale and criteria are unclear because the available deep learning methodologies are mainly black-box models. It is difficult to extract such knowledge from a deep learning model [14].

In this study, we used a data clustering method to overcome these issues, which is a type of unsupervised ML technique. Given a single M-NBI image, the proposed method divides it into several segments and then identifies the clusters in which segments with relevant features are densely located. Consequently, the boundary between the gastric cancer lesions and background mucosa, the DL, can be identified only with the given data. The diagnosis rationale or criteria can be interpreted following the determination of the DL because we specify the potentially discriminating features of gastric cancer before performing the data clustering. Furthermore, the proposed method does not require any annotations or computational effort. Thus, the approach can be applied to determine the DL for early gastric cancer diagnosis and to advance the artificial intelligence (AI)-based diagnostic system.

2. Methods

2.1. Proposed Method

A schematic of the proposed method is presented in Figure 1. It mainly consists of the following four steps: (1) image segmentation, (2) feature extraction, (3) segment-based clustering, and (4) identification of DL candidates. First, an input M-NBI image is segmented into a certain number of superpixels, each set of pixels with similar color features. Second, the image features, including the colors and texture features, are calculated for each superpixel. Third, the superpixels are grouped into a predetermined number of clusters using a data clustering method. Finally, the boundaries of the multiple clusters are extracted as the DL candidates and are presented to the users of the proposed system (endoscopists). The majority of data clustering methods divide the dataset into clusters to minimize the intracluster distance or/and maximize the intercluster distance. Therefore, we hypothesized that the DL could be extracted as the boundary of the clusters because the cancer lesions that would have different image features from the non-cancer lesions should form the cluster. Note that our system was designed to identify only the DL ‘candidates’, so it does not require image annotation by endoscopists. The final decision of

selecting the DL from the candidates is the responsibility of the user endoscopists. The details of each of the four steps are described in the following sections.

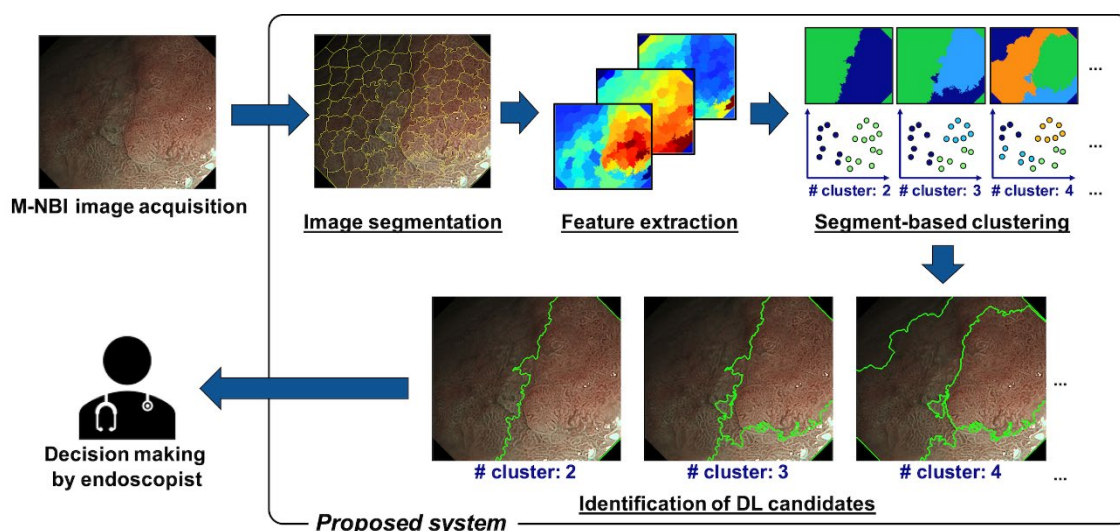


Figure 1. A framework for the proposed method.

2.1.1. Image Segmentation

Several superpixel algorithms have been presented that partition an image into multiple segments. In this study, we used simple linear iterative clustering (SLIC) [18], which is one of the most popular methods in image processing. In the SLIC algorithm, a group of pixels that are similar in terms of both their color features and position (coordinates) is formed as a superpixel. The boundary shapes of the superpixels are iteratively refined by means of the well-known k -means-based clustering approach. First, the input image is divided into a certain number of grids. The center of each tile (the initial form of a superpixel) is sampled and then moved to the pixel with the lowest color gradient among the neighboring pixels. Thereafter, for each pixel in the entire image, the nearest center pixel in terms of both the color and coordinate spaces is searched, and it is assigned to the member of the identified pixel. This procedure is repeated until certain types of termination criteria are satisfied, so that the superpixels are generated. For further details on SLIC, please refer to the original paper [18]. In this study, we used the *slic* function implemented in scikit-image, which is a Python library.

Prior to applying the SLIC image segmentation, we had to determine the color space to represent the image feature. In this study, we employed the International Commission on Illumination (CIE) $L^*a^*b^*$ color space as the image features for segmentation because it is device independent and matches human color perception. It is represented by three-dimensional space consisting of L^* , which represents darkness to lightness; a^* , which varies from red to green; and b^* , which varies from blue to green [19].

2.1.2. Feature Extraction and Clustering

After segmenting an input M-NBI image into a set of superpixels, they are further merged into the clusters of the superpixels using the k -means method. That is, the local clustering of the pixels to extract the pixel-level image feature is performed by SLIC, following which the global clustering of the superpixels is further performed by the k -means method. In the global clustering process, the aim is to identify a cluster of cancer lesions by evaluating each superpixel in terms of both its color and texture features.

The CIE $L^*a^*b^*$ and HSV color spaces were used to represent the color features. The HSV color space is defined by three components: hue, saturation, and value. Hue represents the color type (for example, red, blue, and yellow) ranging from 0 to 360 degrees, saturation represents the color vividness ranging from 0 to 100%, and value represents the

color brightness from 0 to 100% [20]. The coordinates in both color spaces can be calculated by nonlinear transformation from the RGB color space.

In addition to the color features, we aimed to extract the texture features of gastric cancer lesions. Yao et al. [3] set their criterion for early gastric carcinoma as (1) the presence of an irregular microvascular pattern or (2) the presence of an irregular microsurface pattern, both of which were accompanied by a clear DL. Therefore, we expected that the texture features of a gastric cancer lesion could be extracted if the irregularities of the microvascular and microsurface patterns were quantified. We used the local entropy, which quantifies the complexity, such as the randomness of the image, proposed by Wu et al. [21]. The local entropy score $H(S)$ of the image block S (corresponding to a superpixel in this study) in each image can be defined by:

$$H(S) = -\sum_{l=0}^{L-1} P_l \log_2 P_l = -\sum_{l=0}^{L-1} \frac{n_l}{T} \log_2 \frac{n_l}{T}, \quad (1)$$

where $l \in \{0, 1, \dots, L-1\}$ denotes the pixel intensity scale (for example, $L = 256$ for an 8-bit grayscale image) and n_l , T , and P_l denote the total number of pixels within S at pixel intensity l , the total number of pixels, and the probability of a pixel having the intensity l , respectively. In brief, the entropy used in this case quantifies the variability of the pixel values in the image. That is, we assumed that the irregularities of the microvascular and microsurface patterns could be represented by the probability distribution of the pixel values. Note that we calculated the local entropy score for each color dimension.

In total, we used 12-dimensional feature vectors (that is, the six color dimensions L^* , a^* , b^* , H , S , and V and the local entropy score for each of the six color dimensions) for the global clustering by the k -means method. We used the *KMeans* function implemented in scikit-learn.

2.1.3. Identification of DL

Following the global clustering of the superpixels, the boundaries of the clusters are extracted as the DL candidates and are presented on the graphical user interface for the user endoscopists. As mentioned, our system is designed to provide the DL candidates and not to determine the exact DL. The final decision on the DL determination is made by the endoscopists by selecting one of the candidates. In this situation, it is necessary to provide a variety of candidates for the users. Therefore, global clustering with different numbers of clusters (the control parameter k of the k -means method) was executed to provide the DL candidates at different segmentation levels of the M-NBI image. Examples of the cluster boundaries identified following the global clustering are illustrated in Figure 2.

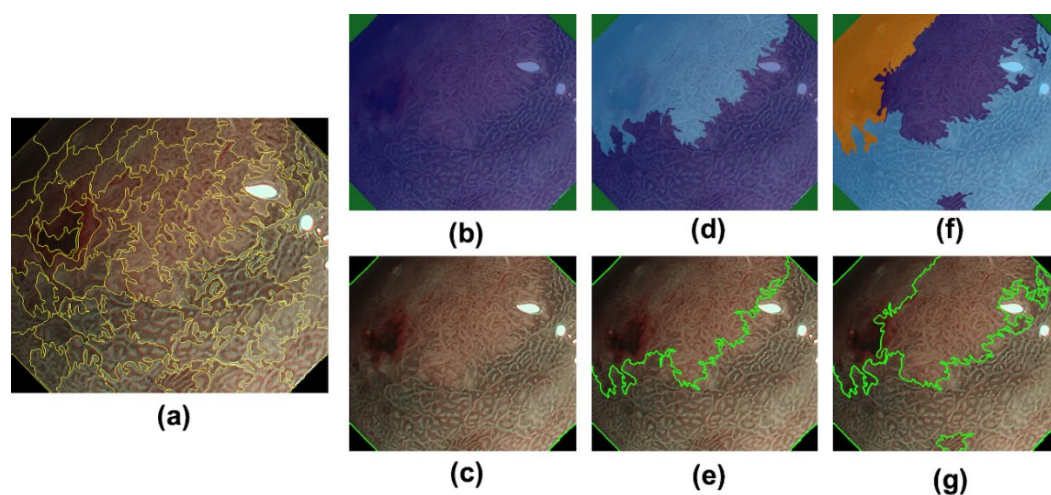


Figure 2. Examples of cluster boundaries identified after global clustering: (a) superpixels identified by local clustering, (b) clusters of superpixels ($k = 2$), where each cluster is painted with a different

color, (c) cluster boundaries ($k = 2$), (d) clusters of superpixels ($k = 3$), (e) cluster boundaries ($k = 3$), (f) clusters of superpixels ($k = 4$), and (g) cluster boundaries ($k = 4$).

2.2. Experimental Setup

To evaluate how accurately our system could provide the DL candidates, we compared them with DLs identified by endoscopists.

2.2.1. Test Images

A total of 23 gastric M-NBI images of 11 cases captured at the Asahi University Hospital, Gifu, Japan, from October 2011 to December 2015 were used for the performance evaluation. Those images were anonymized for personal information, which is not specified. On using still images in this study, all patients provided their written informed consent. Furthermore, the opt-out method was adopted for this retrospective study. The study was approved by the ethics committee of Asahi University Hospital (registration number: 2020-05-01) and was conducted in accordance with the Helsinki Declaration of the World Medical Association and the Ethical Guidelines for Medical and Health Research Involving Human Subjects established by the Ministry of Health, Labour and Welfare, Japan.

All examinations were carried out using the EVIS LUCERA or EVIS LUCERA ELITE systems and the upper gastrointestinal endoscopes GIF-FQ260Z or GIF-H290Z (Olympus Medical Systems, Co., Ltd., Tokyo, Japan). These endoscopic systems have normal white light observation and NBI modes. All images were acquired in the NBI mode, combined with magnifying endoscopy. The clinical characteristics of the patients with early gastric cancer are summarized in Table 1. The resolutions of these images are summarized in Table 2. Moreover, board-certified gastroenterologists at Asahi University Hospital had drawn the DLs on these images. The single expert endoscopist with the most years of experience in endoscopic diagnosis at the Asahi University Hospital drew the DLs, which were assessed by multiple doctors. An example of a DL drawn by an endoscopist is presented in Figure 3.

Table 1. Clinical features of patients included in test images.

Characteristic	Value
Male/female, n	6/5
Age, mean, (range), years	74 (59–92)
Tumor size, Average, (range), mm	
Major axis	14.5 (5–30)
Minor axis	8.8 (4–15)
Tumor location, n	
Upper	1
Middle	3
Lower	7
Morphologic types, n	
Type 0–I	0
Type 0–IIa	3
Type 0–IIb	2
Type 0–IIc	6
Type 1–4	0
Depth of tumor, n	
T1a (mucosa)	10
T1b (submucosa)	1
T2 (muscularis propria) or more	0
Histological classification, n	

Differentiated type	11
Undifferentiated type	0
<i>Helicobacter pylori</i> (<i>H. pylori</i>) status	
Current infection	3
Past infection	8
Atrophic border	
Closed type	2
Open type	9

Table 2. Resolutions of the test images.

CASE	Image Size (Pixels)
	Width ($\mu \pm \sigma$)/Height ($\mu \pm \sigma$)
1 ($n = 4$)	886.8 \pm 2.2/767.8 \pm 1.7
2 ($n = 3$)	887.0 \pm 1.7/768.0 \pm 1.7
3 ($n = 4$)	1041.0 \pm 0.0/901.8 \pm 0.5
4 ($n = 5$)	887.0 \pm 1.2/767.6 \pm 1.3
5 ($n = 1$)	816.0 \pm 0.0/692.0 \pm 0.0
6 ($n = 1$)	832.0 \pm 0.0/760.0 \pm 0.0
7 ($n = 1$)	799.0 \pm 0.0/691.0 \pm 0.0
8 ($n = 1$)	839.0 \pm 0.0/720.0 \pm 0.0
9 ($n = 1$)	752.0 \pm 0.0/602.0 \pm 0.0
10 ($n = 1$)	800.0 \pm 0.0/650.0 \pm 0.0
11 ($n = 1$)	717.0 \pm 0.0/515.0 \pm 0.0

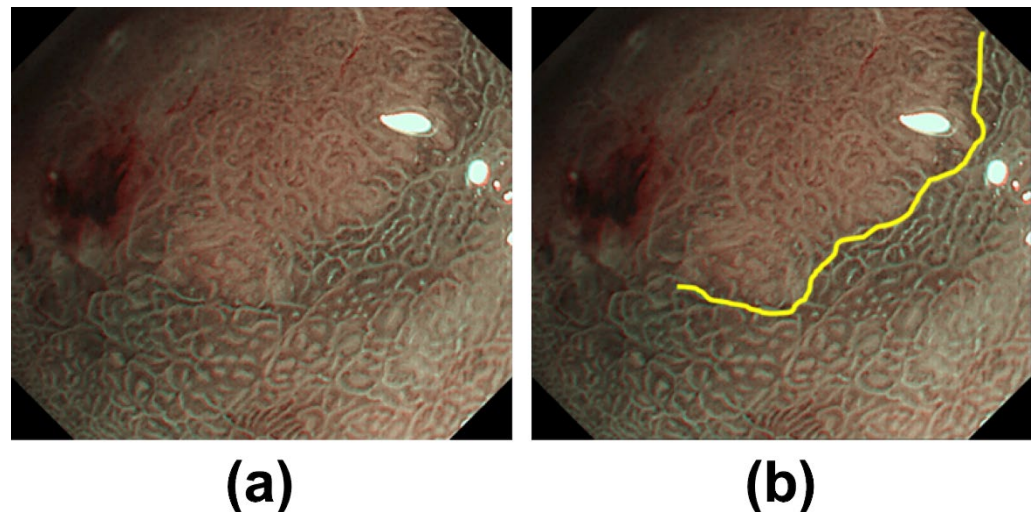


Figure 3. Image with DL drawn by an experienced endoscopist: (a) raw M-NBI image and (b) M-NBI image with DL.

Here it should be noted that the pathological evaluation was carried out using the CASE-11 image. The histopathological image of the resected specimen of CASE 11 was also captured. To pathologically evaluate the proposed system, the M-NBI image of CASE 11 overlapped with the histopathological image of the resected sections and the stereomicroscopic image with a similar field of view (FOV) as the M-NBI image. With these images, we visually investigated whether the proposed method was able to give the boundary between the cancer lesions and background mucosa.

2.2.2. Parameter Settings of the Proposed Method

For the SLIC during the local clustering process, the number of segments (superpixels) of a given image, the '*compactness*' parameter, which controls the balance between the color and space proximity, and the '*sigma*' parameter, which indicates the width of the Gaussian smoothing kernel for each color dimension, were set to 100, 5, and 5 for L^* , a^* , and b^* , respectively. Moreover, for the global clustering process, the maximum number of iterations of the k -means algorithm for a single run was set to 300. The initial cluster centers were determined by the k -means++ algorithm to accelerate convergence. The execution was carried out with different k settings: $k = 2, 3, 4, 5$, and 6. Then, since the clustering result by k -means depends on the first data point chosen as the centroid for each cluster, it was performed for 10 trials for each k setting. The best clustering result that indicated the minimum value of the inertia, the sum of squared distances of samples to their nearest cluster center, was chosen as the DL candidate.

2.2.3. Performance Metrics

We aimed to investigate the similarity between the DLs identified by endoscopists and the proposed method. Therefore, we calculated the Euclidean distance from each pixel of the DL provided by the endoscopist to the nearest pixel of the DL candidates identified by the proposed method as a performance index. All image sizes were adjusted to 564×515 to enable a fair comparison in the Euclidean distance calculation.

3. Results

Figure 4 presents the DL candidates provided by the proposed method with different settings of the number of clusters ($k = 2, 3, 4, 5$, and 6) for each of the 23 M-NBI images obtained from 11 cases. The leftmost image includes the DL provided by the endoscopist. The Euclidean distance between the true DL and DL candidates provided by the proposed method is indicated below each image at different k values. The average computational time for a single image at each k setting was 6.13 ± 1.39 s using an Intel® Core i5 CPU @ 3.30 GHz and DDR3 RAM of 32 GB. The result indicated that our proposed system could generate the DL candidates within a reasonable time.

Case	Endoscopist	k = 2	k = 3	k = 4	k = 5	k = 6	Average	Min.	Max.	
CASE 1	1							70.06	14.07	178.57
			178.57	106.16	37.43	14.07	14.07			
	2							66.43	10.41	163.48
			163.48	97.95	27.35	32.97	10.41			
3							51.92	9.72	182.24	
		182.24	47.19	10.72	9.72	9.72				
4							82.13	8.39	220.29	
		220.29	137.37	22.30	22.30	8.39				
		Case-wise average					67.64	10.65	186.15	
CASE 2	1							61.98	6.24	135.84
			135.84	106.02	52.80	8.98	6.24			
	2							80.03	22.90	236.54
		236.54	89.62	22.90	26.86	24.22				
3							59.75	6.77	247.89	
		247.89	16.74	16.74	10.62	6.77				
		Case-wise average					67.25	11.97	206.76	
CASE 3	1							67.18	9.25	219.16
			219.16	61.23	32.54	9.25	13.74			
	2							73.70	11.94	186.26
			186.26	141.18	16.65	12.45	11.94			
3							49.54	4.70	224.12	
		224.12	6.49	6.49	4.70	5.90				
4							54.87	5.40	228.38	
		228.38	12.66	16.87	11.05	5.40				
		Case-wise average					61.32	7.82	214.48	
CASE 4	1							80.93	7.85	243.15
			243.15	124.02	13.70	15.93	7.85			
	2							82.28	7.87	187.00
			187.00	128.23	7.87	44.51	43.78			
	3							61.34	9.29	131.81
		131.81	123.95	32.34	9.29	9.29				
4							87.15	6.08	213.01	
		213.01	203.22	6.08	6.08	7.35				
5							56.65	11.19	226.81	
		226.81	16.74	16.29	11.19	12.22				
		Case-wise average					73.67	8.46	200.36	
CASE 5							24.10	8.59	58.51	
		58.51	22.58	21.73	9.10	8.59				
CASE 6							49.27	9.72	106.62	
		106.62	106.23	10.95	12.82	9.72				
CASE 7							78.91	12.20	222.72	
		222.72	107.66	26.01	25.95	12.20				
CASE 8							50.59	9.06	177.37	
		177.37	43.62	10.77	12.12	9.06				
CASE 9							29.24	22.86	40.07	
		40.07	33.37	25.20	24.72	22.86				
CASE 10							67.51	8.45	277.31	
		277.31	30.56	12.77	8.47	8.45				
CASE 11							73.06	25.36	102.38	
		102.38	97.55	97.55	42.47	25.36				

Figure 4. DL candidates provided by the proposed method at different cluster number settings ($k = 2, 3, 4, 5,$ and 6) for 23 M-NBI images obtained from 11 cases. The leftmost images present the DLs provided by the endoscopists. The Euclidean distance between the true DL and DL candidates provided by the proposed method is indicated below each image at different k values. The average, minimum, and maximum distances were calculated with different k settings for each case.

Moreover, the images including the nearest DL candidate to the DL drawn by the endoscopist (that is, where the proposed method provided the best performance) are enclosed by blue lines, whereas the maximum ones are enclosed by red lines. Notably, the average minimum Euclidean distance for CASE 1, CASE 2, CASE 3, and CASE 4 were 10.65, 11.97, 7.82, and 8.46, respectively. Additionally, the minimum Euclidean distance for the single-sample cases: CASE5, CASE6, CASE7, CASE8, CASE9, CASE10, and CASE11 was 8.59, 9.72, 12.20, 9.06, 22.86, 8.45, and 25.36, respectively.

Figure 5 indicates the dependence of the Euclidean distance between the DLs provided by the endoscopists and the proposed method on the number of clusters. The dashed black lines correspond to all the images for all cases. The average distance for all images at each k value was calculated and is plotted with a blue point, and these points are connected with a dashed blue line. The average values for $k = 2, 3, 4, 5,$ and 6 were 190.13, 87.12, 20.93, 15.68, and 11.99, respectively.

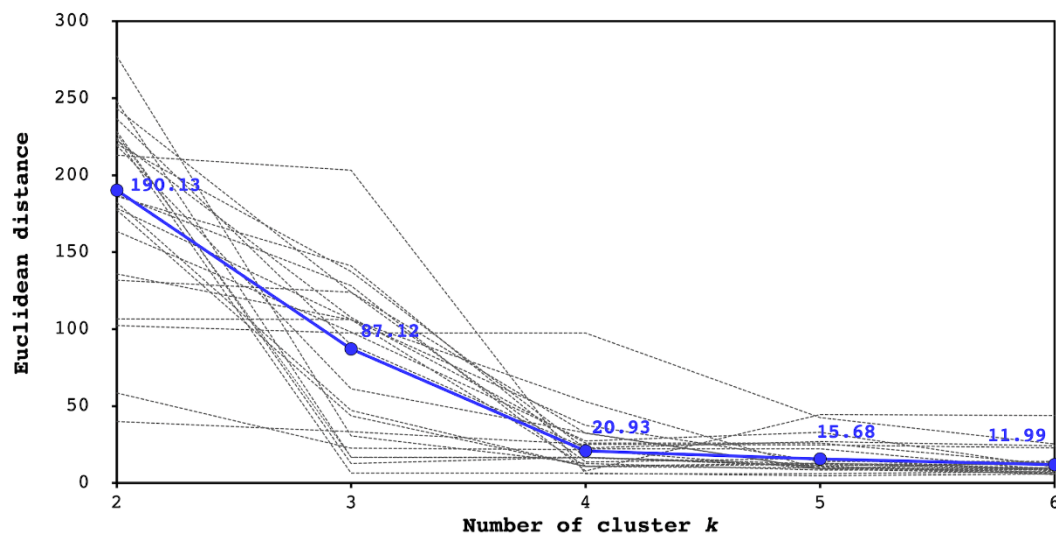


Figure 5. Dependence of Euclidean distance between DLs provided by endoscopists and proposed method on the number of clusters. Each black dashed line indicates the Euclidean distance at each k value for each case. The average distance for all the images at each k value was calculated and is plotted with a blue point, and the points are connected with a dashed blue line.

To pathologically evaluate the proposed system, the M-NBI image of CASE 11 was overlapped with the histopathological image of the resected sections and the stereomicroscopic image with a similar field of view (FOV) as the M-NBI image, as indicated in Figure 6. Figure 6a shows the dependence of the Euclidean distance between DLs provided by endoscopists and the proposed method on the number of clusters, k . Figure 6b indicates the stereomicroscopic image, overlapped with the hematoxylin-and-eosin (H&E) stained tissue sections #1 and #2 of CASE 11. The cut surfaces #1 and #2 correspond to the cutting lines #1 and #2 shown in Figures 6c,d. In Figure 6c, the cancer lesions on cutting lines #1 and #2 were colored red. The yellow dashed lines were the DLs given by the endoscopists, and the green lines were given by the proposed system. The DLs given by the proposed system in Figure 6d resulted in k having a value between 2 and 20. Additionally, each cluster was colored differently in Figure 6d. Furthermore, for $k = 20$ indicated minimum values of the Euclidean distance (Figure 6a), the clustering results around the cutting lines #1 and #2 were clipped out to observe the shape of the clusters and their correspondence to the cancer lesions as shown in Figure 6e.

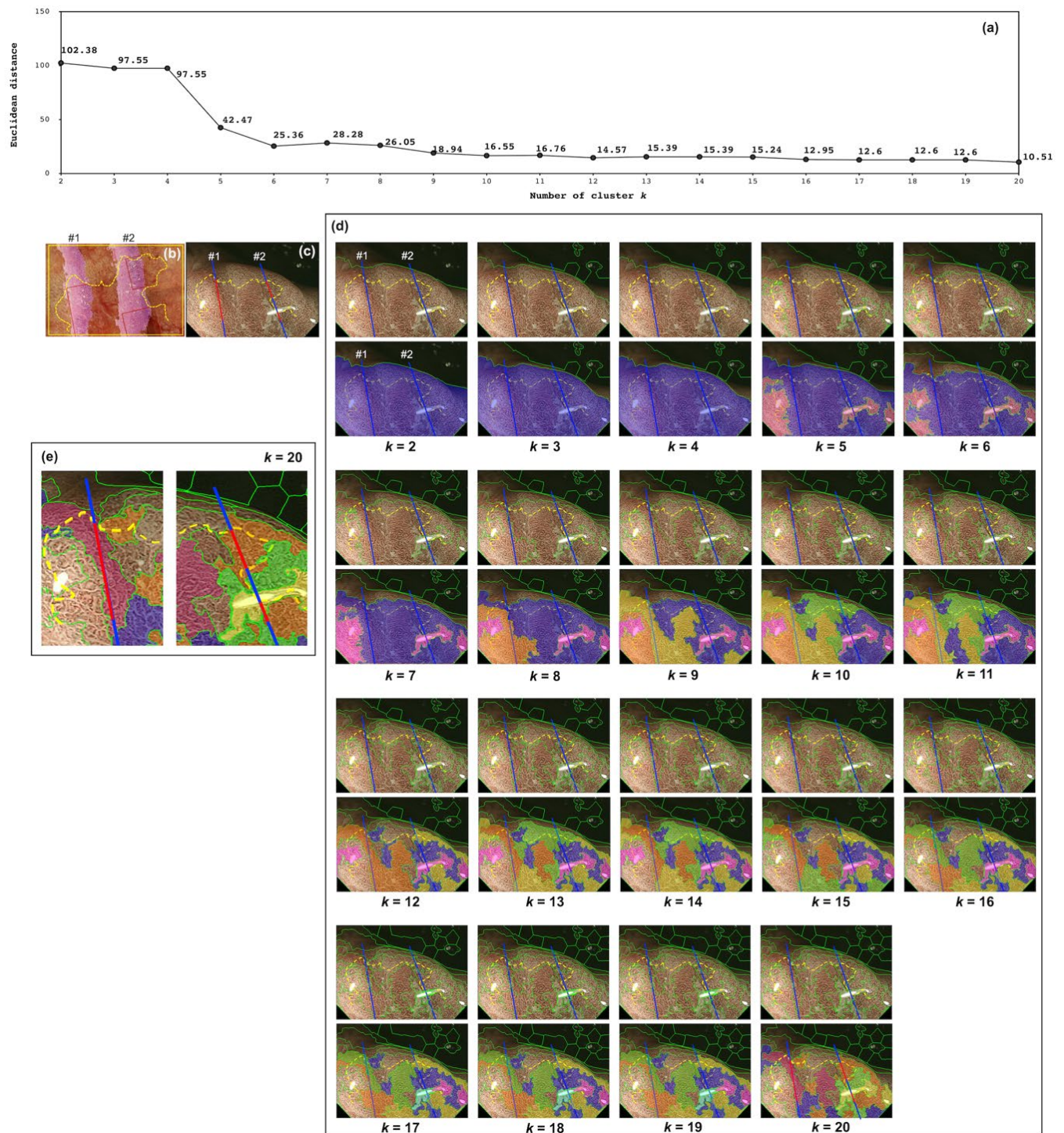


Figure 6. Pathological evaluation of the proposed system for CASE 11. (a) Dependence of the Euclidean distance between DLs provided by endoscopists and their proposed method on the number of clusters, k . (b) Shows a stereomicroscopic image of CASE 11 overlapped with the H&E-stained tissue sections #1 and #2 of CASE 11. The cancer lesion is indicated in the red box. The yellow dashed line is the DL provided by the endoscopist. (c) The cancer lesions on cutting lines #1 and #2 were colored red, otherwise colored blue. (d) In addition to (c), the DLs provided by the proposed system for different k choices ($k = 2, 3, \dots, 20$) are indicated by the green lines in the upper figures. For each k , each of the clusters around the cutting lines is shown in a different color from the other clusters in the lower figures. (e) For $k = 20$ in (d), the clustering results around the cutting lines #1 and #2 are clipped out to observe the shape of the clusters and their correspondence to the cancer lesions.

4. Discussion

4.1. Comparison between the Endoscopists and the Proposed System

It can be observed from Figure 4 that the different cluster number settings resulted in varying shapes of the DL candidates, and the distance to the DL provided by the endoscopist varied accordingly. Furthermore, Figure 5 indicates that the DL candidates provided by the proposed method become more similar to the endoscopist's identification with an increase in the number of clusters. In most cases, the changes in the Euclidean distance were remarkable when k ranged from two to four and were saturated at $k \geq 4$. The approximation accuracy was improved with an increase in the number of clusters because the complexity of the boundary shape increased. These results suggest that the proposed method could identify DL candidates that sufficiently approximated the endoscopist criteria at $k = 4$.

We observed several typical cases of the identified DL candidates to confirm the above assumption. Figure 7a presents the DL candidates identified by the proposed method for CASE 4. At $k = 2$, the cluster boundary was drawn between the field of view (FOV) and the black corner. At $k = 3$, although the boundary was added to the FOV, it simply divided the FOV into two regions where the brightness of the clusters was differentiated. At $k = 4$, the boundary was finally drawn between the clusters with different mucosal patterns. It can be observed that the DL candidate at $k \geq 4$ overlapped the DL provided by the endoscopist. These results visually confirm the assumption that our proposed method could sufficiently approximate the endoscopist criteria at $k = 4$.

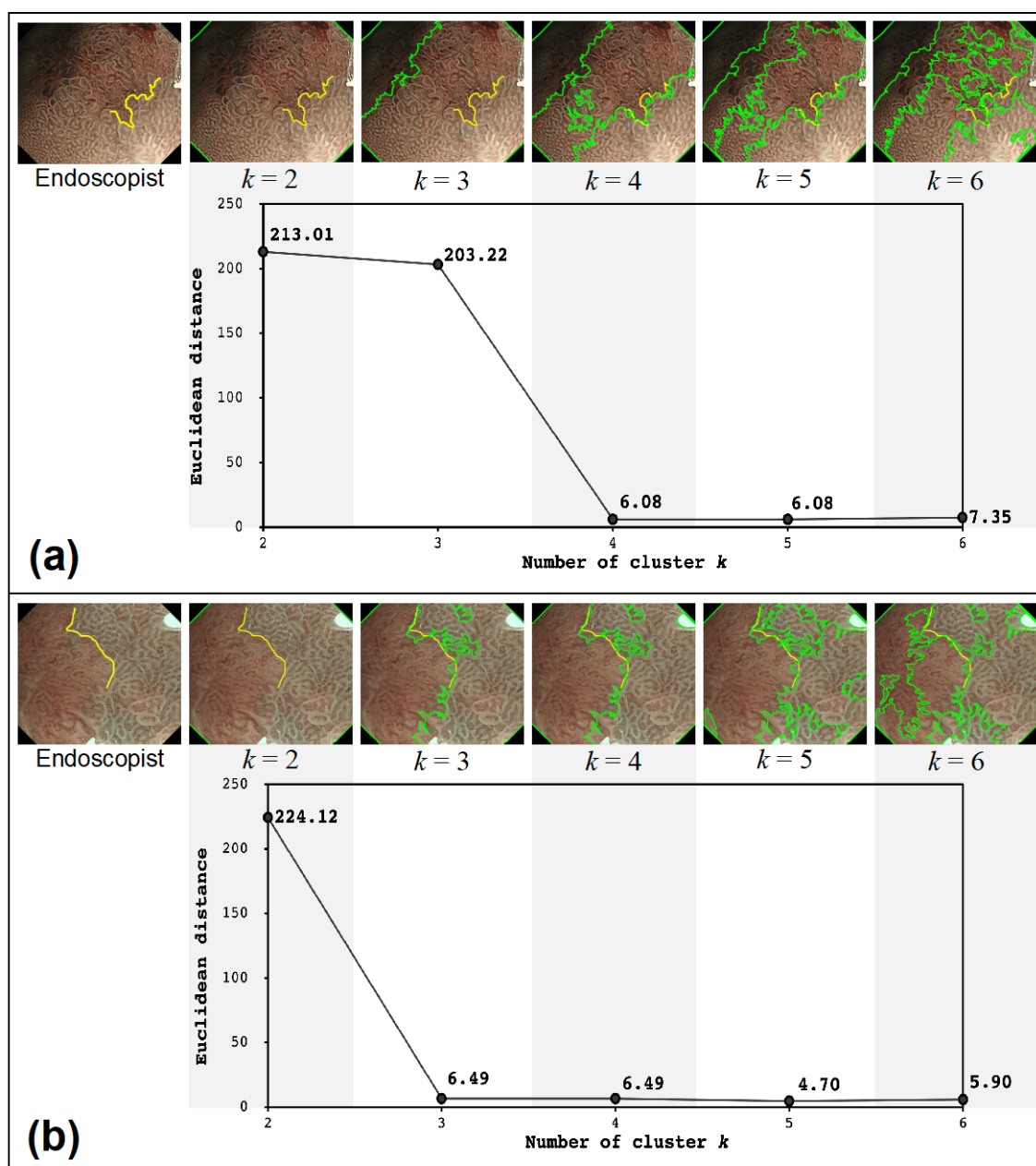


Figure 7. DL candidates identified by the proposed method for (a) CASE 4 and (b) CASE 3. The upper images present the DL candidates at each k value for each subfigure. The yellow and green lines indicate the DLs provided by the endoscopists and the proposed system, respectively. The lower plot shows the dependence of the Euclidean distance between the DLs provided by the endoscopists and the proposed method on different k values.

However, as demonstrated by CASE 3 in Figure 7b, when no shaded regions were observed in the M-NBI image, the proposed method approximated the DL drawn by the endoscopist sufficiently at $k = 3$. No further improvements were observed at $k > 3$, as confirmed visually and quantitatively in Figure 7b.

Therefore, it is confirmed that our proposed method could identify the DL similar to that provided by the endoscopist at $k = 4$. As this process depends on the variety of M-NBI images, user endoscopists would select the appropriate one by adjusting the k value. However, observing multiple DL candidates at different k values may offer new insights into endoscopic diagnosis to user endoscopists. Our method can indicate DLs in regions where endoscopists cannot provide a clear demarcation. This is one of the most important contributions of our study.

A further contribution of our study is that it provides the boundary ‘line’ itself, instead of indicating the cancer lesions as a ‘region’. For example, Li et al. [22] divided M-NBI images into non-cancerous and early gastric cancer groups using a convolutional neural network, one of the most well-known deep learning models. Moreover, Kanesaka et al. [23] detected cancer lesions using the support vector machine. Although they used a supervised ML method, they also aimed to obtain the cancer lesion ‘region’. Providing a ‘line’ rather than a ‘region’ using a CAD system enriches the knowledge of both inexperienced and experienced endoscopists.

In determining the horizontal extent of early gastric mucosal cancer using M-NBI, it is necessary to identify the DL to differentiate the mucosal patterns between cancer lesions and background mucosa. Consequently, the DL exhibits a complex geometric shape, as illustrated in Figure 8. CASE 4 in Figure 8a included depressed lesions, and the endoscopist indicated the DL on the boundary between the depressed lesion and background mucosa. Moreover, Figure 8c indicates that the DL was drawn by tracing the light blue crest in CASE 3. In both cases, the endoscopists drew the DLs to trace the structural change in the white zone, and the DLs resulted in an intricate shape being formed. Notably, our proposed system could precisely provide these irregular and complex shapes, as illustrated in Figure 8b,d.

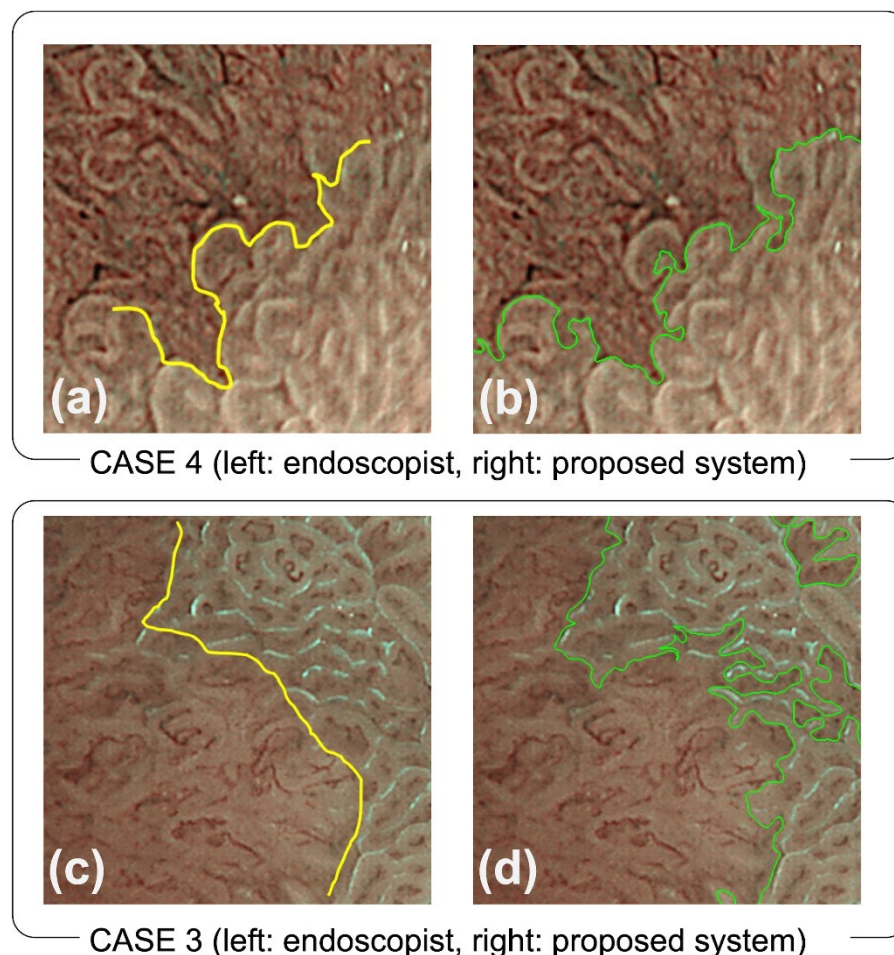


Figure 8. Comparison of DLs provided by the endoscopist and proposed method. The top two images (a,b) indicate the DLs identified by the endoscopist and proposed system, respectively, for CASE 4, whereas the bottom two images (c,d) are for CASE 3.

4.2. Pathological Evaluation of the Proposed System

The proposed system was expected to be able to separate cancerous and noncancerous lesions by cluster boundaries. Therefore, for CASE 11, it was desirable to detect the area corresponding to the red line in Figure 6c as a single cluster. This assumption was confirmed with the results at $k = 20$ in Figures 6d,e. The red line in cutting line #1 was included in the single cluster as shown in the left figure of Figure 6e. Additionally, two cancerous lesions of cutting line #2, indicated by red lines in the right figure of Figure 6e, were part of the orange-colored cluster. It should be noted that this result was not obtained at $k \leq 6$ although the dependence of the Euclidean distance has an inflection point at $k = 6$, as shown in Figure 6a. We concluded that it was due to the existence of the larger shaded regions in CASE 11 than in other cases. The presence of larger shaded regions in the M-NBI image causes them to be segmented in an unnecessary manner. Even at $k \geq 17$, the shape of the clusters in the shared regions varied, as shown in Figure 6d. To overcome this issue, it is necessary to incorporate the predetermination of the regions of interest in the M-NBI images. Nonetheless, increasing the number of clusters, k , confirmed that the current system could generate pathologically valid DL.

However, this study exhibits certain limitations. First, the small sample size ($n = 11$) is problematic. Our system needs to be tested with a larger sample size to improve its reliability and robustness. This work focused on the proposal and development of a general framework for an automatic DL determination algorithm based on a data clustering method. Second, each DL may contain an individual bias because a single endoscopist drew it for each image. Although the DLs were assessed by multiple doctors in the present data, the other DL candidates should be provided by various endoscopists to reduce such bias. Finally, the current study was conducted using only the still M-NBI images. With a recent advance in CAD systems using video images, the future direction should be to investigate the effectiveness of our proposed system using video images. This would also be effective for increasing the sample size. Lastly, the shape of the DL could be affected by the state of *H. pylori* infection, background mucosa, and histological type of cancer. The effects of these factors on the DL determination would be carried out for future studies with larger sample sizes to improve the system's reliability and to proceed to clinical trials. However, irrespective of these limitations, the current results demonstrate the effectiveness of our proposed method and will contribute to the development of gastroenterology.

In summary, we developed a new CAD system that automatically determines the DL on a given M-NBI image through an ML method. In the proposed system, the boundaries of the clusters within M-NBI images are extracted as the DL candidates. The performance evaluation of the system on actual M-NBI images revealed that it could represent the complex shapes of the DLs, similarly to the DLs identified by experienced doctors. The identification of the DL is often quite a difficult task for inexperienced endoscopists. Therefore, our proposed system, which can provide a variety of DL candidates, may support the training of inexperienced doctors as well as enrich the knowledge of experienced doctors.

Author Contributions: S.O. (Conceptualization; Data curation; Formal analysis; Investigation; Methodology; Software; Validation; Visualization; Writing—original draft; Writing—review & editing); M.G. (Conceptualization; Data curation; Formal analysis; Investigation; Methodology; Software; Validation; Visualization; Writing—original draft; Writing—review and editing); S.H. (Conceptualization; Data curation; Formal analysis; Funding acquisition; Investigation; Methodology; Project administration; Resources; Supervision; Visualization; Writing—original draft; Writing—review and editing); T.Y. (Conceptualization; Formal analysis; Investigation; Project administration; Resources; Supervision; Visualization; Writing—original draft; Writing—review and editing); H.K., T.O. and A.T. (Formal analysis; Investigation; Project administration; Resources); Y.Y. (Investigation; Resources); H.I. (Conceptualization; Formal analysis; Investigation; Project administration; Resources; Supervision; Writing—review and editing); N.Y. (Conceptualization; Formal analysis; Investigation; Project administration; Resources; Supervision; Writing—review and editing); T.H. (Conceptualization; Data curation; Formal analysis; Funding acquisition; Investigation;

Methodology; Project administration; Resources; Supervision; Visualization; Writing—original draft; Writing—review and editing). All authors have read and agreed to the published version of the manuscript.

Funding: This research received no external funding.

Institutional Review Board Statement: The study was approved by the ethics committee of Asahi University Hospital (registration number: 2020-05-01) and was conducted in accordance with the Helsinki Declaration of the World Medical Association and the Ethical Guidelines for Medical and Health Research Involving Human Subjects established by the Ministry of Health, Labour and Welfare, Japan.

Informed Consent Statement: On using still images in this study, all patients provided their written informed consent. Furthermore, the opt-out method was adopted for this retrospective study.

Data Availability Statement: All data generated during this study are included in this published article.

Conflicts of Interest: The authors declare that they have no conflict of interest.

References

1. Yao, K. Clinical Application of Magnifying Endoscopy with Narrow-Band Imaging in the Stomach. *Clin. Endosc.* **2015**, *48*, 481–490, <https://doi.org/10.5946/ce.2015.48.6.481>.
2. Ezoe, Y.; Muto, M.; Uedo, N.; Doyama, H.; Yao, K.; Oda, I.; Kaneko, K.; Kawahara, Y.; Yokoi, C.; Sugiura, Y.; et al. Magnifying narrowband imaging is more accurate than conventional white-light imaging in diagnosis of gastric mucosal cancer. *Gastroenterology* **2011**, *141*, 2017–2025.
3. Yao, K.; Anagnostopoulos, G.; Ragunath, K. Magnifying endoscopy for diagnosing and delineating early gastric cancer. *Endoscopy* **2009**, *41*, 462–467.
4. Gotoda, T.; Yamamoto, H.; Soetikno, R.M. Endoscopic submucosal dissection of early gastric cancer. *J. Gastroenterol.* **2006**, *41*, 929–942.
5. Tanaka, M.; Ono, H.; Hasuike, N.; Takizawa, K. Endoscopic submucosal dissection of early gastric cancer. *Digestion* **2008**, *77*, 23–28.
6. Kakushima, N.; Ono, H.; Tanaka, M.; Takizawa, K.; Yamaguchi, Y.; Matsubayashi, H. Factors related to lateral margin positivity for cancer in gastric specimens of endoscopic submucosal dissection. *Dig. Endosc.* **2011**, *23*, 227–232.
7. Sekiguchi, M.; Suzuki, H.; Oda, I.; Abe, S.; Nonaka, S.; Yoshinaga, S.; Taniguchi, H.; Sekine, S.; Kushima, R.; Saito, Y. Risk of recurrent gastric cancer after endoscopic resection with a positive lateral margin. *Endoscopy* **2014**, *46*, 273–278.
8. Kim, T.K.; Kim, G.H.; Park, D.Y.; Lee, B.E.; Jeon, T.Y.; Kim, D.H.; Jo, H.J.; Song, G.A. Risk factors for local recurrence in patients with positive lateral resection margins after endoscopic submucosal dissection for early gastric cancer. *Surg. Endosc.* **2015**, *29*, 2891–2898.
9. Imagawa, A.; Okada, H.; Kawahara, Y.; Takenaka, R.; Kato, J.; Kawamoto, H.; Fujiki, S.; Takata, R.; Yoshino, T.; Shiratori, Y. Endoscopic submucosal dissection for early gastric cancer: results and degrees of technical difficulty as well as success. *Endoscopy* **2006**, *38*, 987–990.
10. Sugimoto, T.; Okamoto, M.; Mitsuno, Y.; Kondo, S.; Ogura, K.; Ohmae, T.; Mizuno, H.; Yoshida, S.; Isomura, Y.; Yamaji, Y.; et al. Endoscopic submucosal dissection is an effective and safe therapy for early gastric neoplasms: a multicenter feasible study. *J. Clin. Gastroenterol.* **2012**, *46*, 124–129.
11. Iizuka, H.; Kakizaki, S.; Sohara, N.; Onozato, Y.; Ishihara, H.; Okamura, S.; Itoh, H.; Mori, M. Stricture after endoscopic submucosal dissection for early gastric cancers and adenomas. *Dig. Endosc.* **2010**, *22*, 282–288.
12. Horie, Y.; Yoshio, T.; Aoyama, K.; Yoshimizu, S.; Horiuchi, Y.; Ishiyama, A.; Hirasawa, T.; Tsuchida, T.; Ozawa, T.; Ishihara, S.; et al. Diagnostic outcomes of esophageal cancer by artificial intelligence using convolutional neural networks. *Gastrointest. Endosc.* **2018**, *89*, 25–32.
13. Hirasawa, T.; Aoyama, K.; Tanimoto, T.; Ishihara, S.; Shichijo, S.; Ozawa, T.; Ohnishi, T.; Fujishiro, M.; Matsuo, K.; Fujisaki, J.; et al. Application of artificial intelligence using a convolutional neural network for detecting gastric cancer in endoscopic images. *Gastric Cancer* **2018**, *21*, 653–660.
14. Yasuda, T.; Hiroyasu, T.; Hiwa, S.; Okada, Y.; Hayashi, S.; Nakahata, Y.; Yasuda, Y.; Omatsu, T.; Obora, A.; Kojima, T.; et al. Potential of automatic diagnosis system with linked color imaging for diagnosis of Helicobacter pylori infection. *Dig. Endosc.* **2020**, *32*, 373–381.
15. Misawa, M.; Kudo, S.-E.; Mori, Y.; Nakamura, H.; Kataoka, S.; Maeda, Y.; Kudo, T.; Hayashi, T.; Wakamura, K.; Miyachi, H.; et al. Characterization of Colorectal Lesions Using a Computer-Aided Diagnostic System for Narrow-Band Imaging Endocytoscopy. *Gastroenterology* **2016**, *150*, 1531–1532.
16. Shichijo, S.; Nomura, S.; Aoyama, K.; Nishikawa, Y.; Miura, M.; Shinagawa, T.; Takiyama, H.; Tanimoto, T.; Ishihara, S.; Matsuo, K.; et al. Application of Convolutional Neural Networks in the Diagnosis of Helicobacter pylori Infection Based on Endoscopic Images. *eBioMedicine* **2017**, *25*, 106–111.

17. Mori, Y.; Kudo, S.; Mohmed, H.E.N.; Misawa, M.; Ogata, N.; Itoh, H.; Oda, M.; Mori, K. Artificial intelligence and upper gastrointestinal endoscopy: Current status and future perspective. *Dig. Endosc.* **2018**, *31*, 378–388.
18. Achanta, R.; Shaji, A.; Smith, K.; Lucchi, A.; Fua, P.; Süsstrunk, S. SLIC Superpixels Compared to State-of-the-Art Superpixel Methods. *IEEE Trans. Pattern Anal. Mach. Intell.* **2012**, *34*, 2274–2282.e3.
19. Wyszecki, G.; Stiles, W.S. *Color Science*; Wiley: New York, NY, USA, 1982; Volume 8.
20. Agoston, M.K.; Agoston, M.K. *Computer Graphics and Geometric Modeling*; Springer: London, UK, 2005; Volume 1.
21. Wu, Y.; Zhou, Y.; Saveriades, G.; Agaian, S.; Noonan, J.P.; Natarajan, P. Local Shannon entropy measure with statistical tests for image randomness. *Inf. Sci.* **2013**, *222*, 323–342.
22. Li, L.; Chen, Y.; Shen, Z.; Zhang, X.; Sang, J.; Ding, Y.; Yang, X.; Li, J.; Chen, M.; Jin, C.; et al. Convolutional neural network for the diagnosis of early gastric cancer based on magnifying narrow band imaging. *Gastric Cancer* **2019**, *23*, 126–132.
23. Kanesaka, T.; Lee, T.-C.; Uedo, N.; Lin, K.-P.; Chen, H.-Z.; Lee, J.-Y.; Wang, H.-P.; Chang, H.-T. Computer-aided diagnosis for identifying and delineating early gastric cancers in magnifying narrow-band imaging. *Gastrointest. Endosc.* **2018**, *87*, 1339–1344.